

**Measurement of the  $\eta \rightarrow \pi^+\pi^-\pi^0$  Dalitz plot distribution**

P. Adlarson,<sup>1</sup> W. Augustyniak,<sup>2</sup> W. Bardan,<sup>3</sup> M. Bashkanov,<sup>4,5</sup> F. S. Bergmann,<sup>6</sup> M. Berłowski,<sup>7</sup> H. Bhatt,<sup>8</sup> A. Bondar,<sup>9,10</sup> M. Büscher,<sup>11,12,\*</sup> H. Calén,<sup>1</sup> I. Ciepiał,<sup>3</sup> H. Clement,<sup>4,5</sup> D. Coderre,<sup>11,12,13,†</sup> E. Czerwiński,<sup>3</sup> K. Demmich,<sup>6</sup> E. Doroshkevich,<sup>4,5</sup> R. Engels,<sup>11,12</sup> A. Erven,<sup>12,14</sup> W. Erven,<sup>12,14</sup> W. Eyrych,<sup>15</sup> P. Fedorets,<sup>11,12,16</sup> K. Föhl,<sup>17</sup> K. Fransson,<sup>1</sup> F. Goldenbaum,<sup>11,12</sup> P. Goslawski,<sup>6</sup> A. Goswami,<sup>11,12,18</sup> K. Grigoryev,<sup>11,12,19,‡</sup> C.-O. Gullström,<sup>1</sup> F. Hauenstein,<sup>15</sup> L. Heijkenkjöld,<sup>1</sup> V. Hejny,<sup>11,12</sup> M. Hodana,<sup>3</sup> B. Höistad,<sup>1</sup> N. Hüskens,<sup>6</sup> A. Jany,<sup>3</sup> B. R. Jany,<sup>3</sup> L. Jarczyk,<sup>3</sup> T. Johansson,<sup>1</sup> B. Kamys,<sup>3</sup> G. Kemmerling,<sup>12,14</sup> F. A. Khan,<sup>11,12</sup> A. Khoukaz,<sup>6</sup> D. A. Kirillov,<sup>20</sup> S. Kistryn,<sup>3</sup> H. Kleines,<sup>12,14</sup> B. Klos,<sup>21</sup> W. Krzemień,<sup>3</sup> P. Kulesa,<sup>22</sup> A. Kupś,<sup>1,7</sup> A. Kuzmin,<sup>9,10</sup> K. Lalwani,<sup>8,§</sup> D. Lersch,<sup>11,12</sup> B. Lorentz,<sup>11,12</sup> A. Magiera,<sup>3</sup> R. Maier,<sup>11,12</sup> P. Marciniwski,<sup>1</sup> B. Mariański,<sup>2</sup> B. V. Martemyanov,<sup>16</sup> U.-G. Meißner,<sup>11,12,23,24,25</sup> M. Mikirtychiants,<sup>11,12,13,19</sup> H.-P. Morsch,<sup>2</sup> P. Moskal,<sup>3</sup> H. Ohm,<sup>11,12</sup> I. Ozerianska,<sup>3</sup> E. Perez del Rio,<sup>4,5</sup> N. M. Piskunov,<sup>20</sup> P. Podkopał,<sup>3</sup> D. Prasuhn,<sup>11,12</sup> A. Pricking,<sup>4,5</sup> D. Pszczel,<sup>1,7</sup> K. Pysz,<sup>22</sup> A. Pysznik,<sup>1,3</sup> C. F. Redmer,<sup>1,||</sup> J. Ritman,<sup>11,12,13</sup> A. Roy,<sup>18</sup> Z. Rudy,<sup>3</sup> S. Sawant,<sup>8,11,12</sup> S. Schadmand,<sup>11,12</sup> T. Sefzick,<sup>11,12</sup> V. Serdyuk,<sup>11,12,26</sup> B. Shwartz,<sup>9,10</sup> R. Siudak,<sup>22</sup> T. Skorodko,<sup>4,5</sup> M. Skurzok,<sup>3</sup> J. Smyrski,<sup>3</sup> V. Sopov,<sup>16</sup> R. Stassen,<sup>11,12</sup> J. Stepaniak,<sup>7</sup> E. Stephan,<sup>21</sup> G. Sterzenbach,<sup>11,12</sup> H. Stockhorst,<sup>11,12</sup> H. Ströher,<sup>11,12</sup> A. Szczurek,<sup>22</sup> A. Täschner,<sup>6</sup> A. Trzciniński,<sup>2</sup> R. Varma,<sup>8</sup> M. Wolke,<sup>1</sup> A. Wrońska,<sup>3</sup> P. Wüstner,<sup>12,14</sup> P. Wurm,<sup>11,12</sup> A. Yamamoto,<sup>27</sup> X. Yuan,<sup>28</sup> L. Yurev,<sup>26,¶</sup> J. Zabierowski,<sup>29</sup> C. Zheng,<sup>28</sup> M. J. Zieliński,<sup>3</sup> A. Zink,<sup>15</sup> J. Złomańczuk,<sup>1</sup> P. Żuprański,<sup>2</sup> and M. Żurek<sup>11,12</sup>  
(WASA-at-COSY Collaboration)

<sup>1</sup>Division of Nuclear Physics, Department of Physics and Astronomy, Uppsala University, Box 516, 75120 Uppsala, Sweden

<sup>2</sup>Department of Nuclear Physics, National Centre for Nuclear Research, ul. Hoza 69, 00-681 Warsaw, Poland

<sup>3</sup>Institute of Physics, Jagiellonian University, ul. Reymonta 4, 30-059 Kraków, Poland

<sup>4</sup>Physikalisches Institut, Eberhard-Karls-Universität Tübingen, Auf der Morgenstelle 14, 72076 Tübingen, Germany

<sup>5</sup>Kepler Center für Astro- und Teilchenphysik, Physikalisches Institut der Universität Tübingen, Auf der Morgenstelle 14, 72076 Tübingen, Germany

<sup>6</sup>Institut für Kernphysik, Westfälische Wilhelms-Universität Münster, Wilhelm-Klemm-Strasse 9, 48149 Münster, Germany

<sup>7</sup>High Energy Physics Department, National Centre for Nuclear Research, ul. Hoza 69, 00-681 Warsaw, Poland

<sup>8</sup>Department of Physics, Indian Institute of Technology Bombay, Powai, Mumbai, 400076 Maharashtra, India

<sup>9</sup>Budker Institute of Nuclear Physics of SB RAS, 11 Akademika Lavrentieva Prospect, Novosibirsk 630090, Russia

<sup>10</sup>Novosibirsk State University, 2 Pirogova Strasse, Novosibirsk 630090, Russia

<sup>11</sup>Institut für Kernphysik, Forschungszentrum Jülich, 52425 Jülich, Germany

<sup>12</sup>Jülich Center for Hadron Physics, Forschungszentrum Jülich, 52425 Jülich, Germany

<sup>13</sup>Institut für Experimentalphysik I, Ruhr-Universität Bochum, Universitätsstrasse 150, 44780 Bochum, Germany

<sup>14</sup>Zentralinstitut für Engineering, Elektronik und Analytik, Forschungszentrum Jülich, 52425 Jülich, Germany

<sup>15</sup>Physikalisches Institut, Friedrich-Alexander-Universität Erlangen-Nürnberg, Erwin-Rommel-Strasse 1, 91058 Erlangen, Germany

<sup>16</sup>Institute for Theoretical and Experimental Physics, State Scientific Center of the Russian Federation, Bolshaya Cheremushkinskaya 25, 117218 Moscow, Russia

<sup>17</sup>II. Physikalisches Institut, Justus-Liebig-Universität Gießen, Heinrich-Buff-Ring 16, 35392 Giessen, Germany

<sup>18</sup>Department of Physics, Indian Institute of Technology Indore, Khandwa Road, Indore, 452017 Madhya Pradesh, India

<sup>19</sup>High Energy Physics Division, Petersburg Nuclear Physics Institute, Orlova Roshka 2, Gatchina, Leningrad district 188300, Russia

<sup>20</sup>Veksler and Baldin Laboratory of High Energy Physics, Joint Institute for Nuclear Physics, Joliot Curie 6, 141980 Dubna, Russia

<sup>21</sup>August Chełkowski Institute of Physics, University of Silesia, Uniwersytecka 4, 40-007 Katowice, Poland

<sup>22</sup>The Henryk Niewodniczański Institute of Nuclear Physics, Polish Academy of Sciences, ul. 152 Radzikowskiego, 31-342 Kraków, Poland

<sup>23</sup>Institute for Advanced Simulation, Forschungszentrum Jülich, 52425 Jülich, Germany

<sup>24</sup>Helmholtz-Institut für Strahlen- und Kernphysik, Rheinische Friedrich-Wilhelms-Universität Bonn, Nußallee 14–16, 53115 Bonn, Germany

<sup>25</sup>Bethe Center for Theoretical Physics, Rheinische Friedrich-Wilhelms-Universität Bonn, 53115 Bonn, Germany

<sup>26</sup>Dzhelepov Laboratory of Nuclear Problems, Joint Institute for Nuclear Physics, Joliot Curie 6, 141980 Dubna, Russia

<sup>27</sup>High Energy Accelerator Research Organisation KEK, Tsukuba, Ibaraki 305-0801, Japan

<sup>28</sup>Institute of Modern Physics, Chinese Academy of Sciences, 509 Nanchang Road, Lanzhou 730000, China

<sup>29</sup>Department of Cosmic Ray Physics, National Centre for Nuclear Research, ul. Uniwersytecka 5, 90–950 Łódź, Poland

(Received 11 June 2014; revised manuscript received 29 September 2014; published 29 October 2014)

The Dalitz plot distribution of the  $\eta \rightarrow \pi^+\pi^-\pi^0$  decay is determined by using a data sample of  $1.2 \times 10^7$   $\eta$  mesons from the  $pd \rightarrow {}^3\text{He}\eta$  reaction at 1 GeV collected by the WASA detector at COSY.

DOI: [10.1103/PhysRevC.90.045207](https://doi.org/10.1103/PhysRevC.90.045207)

PACS number(s): 13.25.-k, 13.20.-v, 14.40.Be, 24.85.+p

\*Present address: Peter Grünberg Institut, PGI-6 Elektronische Eigenschaften, Forschungszentrum Jülich, 52425 Jülich, Germany;

Institut für Laser- und Plasmaphysik, Heinrich-Heine Universität Düsseldorf, Universitätsstr. 1, 40225 Düsseldorf, Germany.

## I. INTRODUCTION

The amplitude of the isospin-violating decays  $\eta \rightarrow \pi^+\pi^-\pi^0$  and  $\eta \rightarrow \pi^0\pi^0\pi^0$  is dominated by a term proportional to the light quark mass difference ( $m_d - m_u$ ) since the electromagnetic contribution is suppressed [1–3]. This makes the decays a sensitive probe of the light quark masses [4]. The leading term for the partial decay widths of the two decay modes is proportional to  $Q^{-4}$ , where  $Q^2$  is defined as the following combination of the light quark masses [5]:

$$Q^2 = \frac{m_s^2 - \hat{m}^2}{m_d^2 - m_u^2}, \quad \hat{m} = \frac{1}{2}(m_u + m_d). \quad (1)$$

The determination of the  $Q$  parameter requires knowledge of the experimental value of at least one of the  $\eta \rightarrow \pi^+\pi^-\pi^0$  and  $\eta \rightarrow \pi^0\pi^0\pi^0$  partial decay widths and the corresponding proportionality factors.

Experimental determination of the partial decay widths requires knowledge of the  $\eta$  radiative width,  $\Gamma_{\gamma\gamma}$ , and the relative branching ratios  $BR(\eta \rightarrow \pi^0\pi^0\pi^0)/BR(\eta \rightarrow \gamma\gamma)$  and  $BR(\eta \rightarrow \pi^+\pi^-\pi^0)/BR(\eta \rightarrow \gamma\gamma)$ . The radiative width could be determined by measuring the cross section of the  $\eta$  meson two-photon production using, e.g., the Primakov effect or the  $e^+e^- \rightarrow e^\pm e^- \eta$  process. Knowledge of the Dalitz plot distributions for the  $\eta \rightarrow 3\pi$  decays will in principle contribute to all measurements involving these final states. For example,  $\Gamma_{\gamma\gamma}$  was recently extracted from the cross section of the two-photon production  $e^+e^- \rightarrow e^+e^-\eta$  where the  $\eta$  meson was tagged by the  $\eta \rightarrow \pi^0\pi^0\pi^0$  and  $\eta \rightarrow \pi^+\pi^-\pi^0$  decay modes [6].

The calculations of the proportionality factors could be carried out in the low-energy effective field theory of the strong interactions, chiral perturbation theory (ChPT). The process was calculated up to next-to-next-leading order (NNLO) [7–10]. The ChPT leading order (LO) result together with the measured value of the  $\eta \rightarrow \pi^+\pi^-\pi^0$  decay width of  $300 \pm 12$  eV [11] leads to  $Q = 15.6$  (Table I). The next-to-leading order (NLO) gives a  $Q$  value 28% larger where half of the increase comes from  $\pi\pi$  rescattering between final state pions [9,12]. Finally, the NNLO increases the value by an additional 14%. The values of  $Q$  extracted from various analyses are summarized in Table I.

The reliability of the calculations leading to the proportionality factor could be tested by comparing the experimental and theoretical Dalitz plots for both the neutral and charged modes. Such comparison constitutes a sensitive test of the convergence

TABLE I. Values of  $Q$  obtained from the  $\eta \rightarrow 3\pi$  decay. In addition a lattice QCD estimate is shown for comparison.

Calculations	$Q$
LO [10]	15.6
NLO [10]	20.1
NNLO [10]	22.9
dispersive [13]	22.7(8)
dispersive [14]	22.4(9)
dispersive (PLM) [15]	23.1(7)
lattice QCD avg. [16]	22.6(7)(6)

of the SU(3) ChPT expansion. For the neutral decay mode, where the Dalitz plot density is described by a single parameter up to quadratic terms, the experiments provide a consistent, precise value [17–25]. However, reproduction of this value has turned out to be a challenge for the ChPT calculations. For the  $\eta \rightarrow \pi^+\pi^-\pi^0$  decay mode, where there are more parameters to describe Dalitz plot density, there is basically only one modern, high-statistics experiment [26].

The amplitudes for the  $\eta \rightarrow 3\pi$  decays could be also determined using unitarity and analyticity and the  $\pi\pi$  phase shifts up to some subtraction constants. These subtraction constants can be determined by matching to the results of the ChPT calculations [13,14] and thus improving convergence of the ChPT expansion. Alternatively, the subtraction constants can be obtained directly from fits to the experimental Dalitz plot distributions using only the most reliable constraints from ChPT. In recent years, two such data-driven dispersive approaches have emerged: from the Bern-Lund-Valencia (BLV) group [27] and from the Prague-Lund-Marseille (PLM) group [15]. Both approaches rely to a large extent on the experimental Dalitz plot data and promise a precise determination of  $Q$ .

Other aspects of the  $\eta \rightarrow 3\pi$  decay such as isospin-violation effects in low-energy  $\pi\pi$  scattering are addressed by nonrelativistic effective field theory (NREFT), which was developed first for low-energy  $\pi\pi$  scattering and  $K \rightarrow 3\pi$  [28] decays and subsequently applied to  $\eta \rightarrow 3\pi$  decays [29,30]. A more model-dependent analysis providing uniform treatment of all three pseudoscalar  $\eta$  and  $\eta'$  decay modes, including  $\eta \rightarrow 3\pi$ , was pursued in Ref. [31].

The Dalitz plot for  $\eta \rightarrow \pi^+\pi^-\pi^0$  is expressed by using normalized variables  $X$  and  $Y$ :

$$X = \sqrt{3} \frac{T_+ - T_-}{Q_\eta}; \quad Y = \frac{3T_0}{Q_\eta} - 1, \quad (2)$$

where  $T_+$ ,  $T_-$ , and  $T_0$  are the kinetic energies of the charged and neutral pions in the  $\eta$  meson rest frame.  $Q_\eta$  is the excess energy for the decay:

$$Q_\eta = T_+ + T_- + T_0 \quad (3)$$

or, equivalently,  $Q_\eta = m_\eta - 2m_\pm - m_0$ , where  $m_\pm$  and  $m_0$  are the masses of the charged and neutral pions. A polynomial parametrization is often used to represent the squared amplitude for the decay:

$$|\mathcal{A}(X,Y)|^2 \propto \rho(X,Y) = N(1 + aY + bY^2 + cX + dX^2 + eXY + fY^3 + gX^2Y + hX^3), \quad (4)$$

<sup>†</sup>Present address: Albert Einstein Center for Fundamental Physics, University of Bern, Sidlerstrasse 5, 3012 Bern, Switzerland.

<sup>‡</sup>Present address: III. Physikalisches Institut B, Physikzentrum, RWTH Aachen, 52056 Aachen, Germany.

<sup>§</sup>Present address: Department of Physics and Astrophysics, University of Delhi, Delhi, 110007, India.

<sup>||</sup>Present address: Institut für Kernphysik, Johannes Gutenberg-Universität Mainz, Johann-Joachim-Becher Weg 45, 55128 Mainz, Germany.

<sup>¶</sup>Present address: Department of Physics and Astronomy, University of Sheffield, Hounsfield Road, Sheffield, S3 7RH, United Kingdom.

TABLE II. Dalitz plot parameters from theoretical predictions and experimental results for  $\eta \rightarrow \pi^+\pi^-\pi^0$ . Results at LO, NLO, and NNLO ChPT are taken from [10]. The values inside the parentheses denote the quoted uncertainties. For the KLOE data both statistical and systematic uncertainties are given.

	$-a$	$b$	$d$	$f$	$g$
Calculations					
LO [10]	1.039	0.27	0.000	0.000	—
NLO [10]	1.371	0.452	0.053	0.027	—
NNLO [10]	1.271(75)	0.394(102)	0.055(57)	0.025(160)	—
dispersive [14]	1.16	0.26	0.10	—	—
tree dispersive [32]	1.10	0.31	0.001	—	—
absolute dispersive [32]	1.21	0.33	0.04	—	—
NREFT [30]	1.213(14)	0.308(23)	0.050(3)	0.083(19)	-0.039(2)
BSE [31]	1.054(25)	0.185(15)	0.079(26)	0.064(12)	—
Experiment					
Gormley [33]	1.17(2)	0.21(3)	0.06(4)	—	—
Layter <i>et al.</i> [34]	1.080(14)	0.03(3)	0.05(3)	—	—
CBarrel-98 [35]	1.22(7)	0.22(11)	0.06 (fixed)	—	—
KLOE [26]	1.090(5) <sub>-8</sub> <sup>+19</sup>	0.124(6)(10)	0.057(6) <sub>-16</sub> <sup>+7</sup>	0.14(1)(2)	~0

where  $\rho(X, Y)$  is the Dalitz plot density,  $N$  is a normalization factor, and  $a, b, \dots, g, h$  are *Dalitz plot parameters*. The terms with odd powers of the  $X$  variable, such as  $c, e,$  and  $h$ , should be zero, as they imply charge-conjugation violation in strong or electromagnetic interactions. The Dalitz plot parameters from various theoretical predictions and from experiments are given in Table II.

The best precision in the experimental Dalitz plot parameter values is achieved in the recent KLOE [26] experiment from the analysis of  $1.34 \times 10^6$   $\eta \rightarrow \pi^+\pi^-\pi^0$  decays. The description of the KLOE data requires inclusion of a cubic term (the  $f$  parameter). The quadratic term  $b$  disagrees with the experimental results from the 1970s [33,34], while it agrees with the Crystal Barrel results [35] within uncertainties. A comparison of the KLOE result to the theoretical predictions shows disagreement for both the  $a$  and  $b$  parameter values when taking into account the combined uncertainties of the experimental and theoretical predictions. The discrepancies are more than five standard deviations for the NNLO parameter  $a$  and  $b$  values. Also, model-independent relations between neutral and charged Dalitz plot parameters indicate a tension between the experimental data on the two channels [30].

A solid experimental data base for the Dalitz plot distributions is a must for further more detailed investigations. The next goal is to reach an experimental status for the charged  $\eta \rightarrow \pi^+\pi^-\pi^0$  channel that is comparable to that for the neutral  $\eta \rightarrow \pi^0\pi^0\pi^0$  channel. Therefore, several new high-statistics measurements of the charged channel are required.

Here we present a first step to match the KLOE precision with an independent measurement of the  $\eta \rightarrow \pi^+\pi^-\pi^0$  Dalitz plot parameters.

## II. EXPERIMENT

### A. The WASA detector

The presented results are obtained with the WASA detector [36,37], in an internal target experiment at the cooler synchrotron COSY storage ring [38], Forschungszentrum Jülich,

Germany. The COSY proton beam interacts with an internal target consisting of small pellets of frozen deuterium (diameter  $\sim 35$   $\mu\text{m}$ ). The  $\eta$  mesons for the  $\eta \rightarrow 3\pi$  decay studies were produced using the  $pd \rightarrow {}^3\text{He}\eta$  reaction at a proton kinetic energy of 1 GeV, corresponding to a center-of-mass excess energy of 60 MeV. The cross section of the reaction is 0.40(3)  $\mu\text{b}$  at this energy [39,40].

The WASA detector consists of a central detector (CD) and a forward detector (FD), covering scattering angles of  $20^\circ$ – $169^\circ$  and  $3^\circ$ – $18^\circ$ , respectively, in combination with an almost full azimuthal angle coverage. The CD is used to detect and measure the decay products of the mesons. A straw cylindrical chamber (MDC) is placed in a magnetic field, provided by a superconducting solenoid, for momentum determination of charged particles. The central value of the magnetic field was 0.85 T during the experiment. The electromagnetic calorimeter consists of 1012 CsI(Na) crystals read out by photomultipliers. A plastic scintillator barrel is placed between the MDC and the solenoid, allowing particle identification and accurate timing for charged tracks. The FD consists of 13 layers of plastic scintillators providing energy and time information and a straw tube tracker for precise track reconstruction.

At the trigger level, events with at least one track in the forward detector and with a high energy deposit in the thin plastic scintillator layers were accepted. The condition is effective for selection of  ${}^3\text{He}$  ions and provides an unbiased data sample of  $\eta$  meson decays. The proton beam energy was chosen so the  ${}^3\text{He}$  produced in the  $pd \rightarrow {}^3\text{He}\eta$  reaction stopping in the first thick scintillator layer of the FD.

The  $\Delta E$ - $\Delta E$  correlation plot from a thin layer and the first thick layer of the FD is shown in Fig. 1(a). The (upper) band corresponding to the  ${}^3\text{He}$  ion is well separated from the bands for other particles and allows a clear identification of  ${}^3\text{He}$ . The  ${}^3\text{He}$  ions from the reaction of interest have kinetic energies ranging between 220 and 460 MeV and scattering angles ranging from  $0^\circ$  to  $10^\circ$ .

The missing mass calculated from the reconstructed  ${}^3\text{He}$  momentum,  $\text{MM}({}^3\text{He})$ , is shown in Fig. 1(b). The  $\eta$  peak has

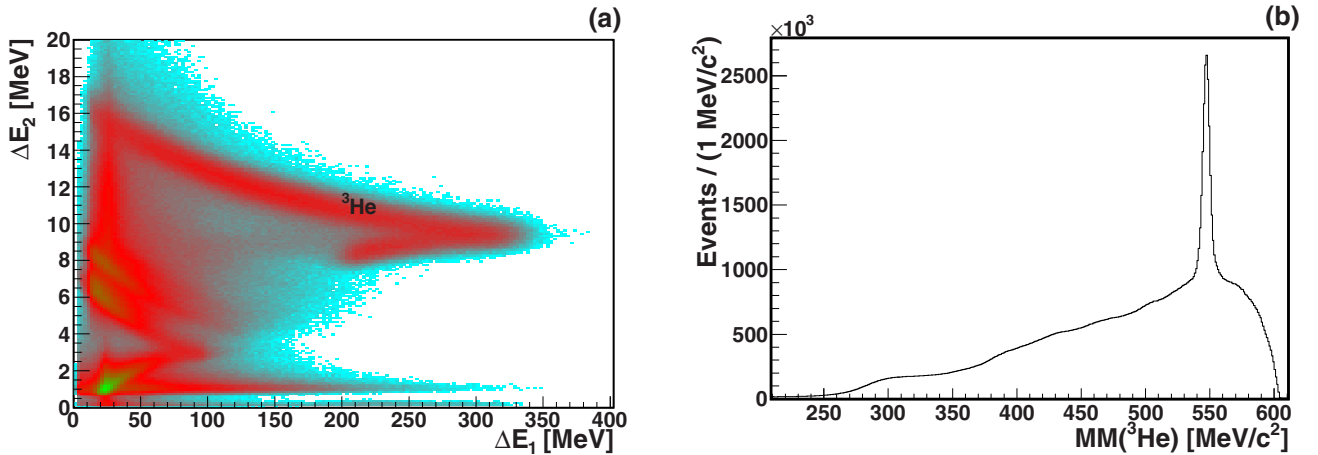


FIG. 1. (Color online) (a) Correlation of energy deposits between two FD plastic detector layers: the first thick layer (11 cm),  $\Delta E_1$ , and a preceding thin (0.5 cm) layer,  $\Delta E_2$ . (b)  $MM(^3\text{He})$  for all events with a  $^3\text{He}$  ion detected in the FD. There are about  $1.2 \times 10^7$  events in the peak corresponding to the  $pd \rightarrow ^3\text{He}\eta$  reaction.

a full width at half maximum (FWHM) of  $6.2 \text{ MeV}/c^2$  and contains about  $1.2 \times 10^7$  events. The luminosity during the run was kept in the range  $(1-5) \times 10^{31} \text{ cm}^{-2} \text{ s}^{-1}$ .

### B. Simulation

The production reaction  $pd \rightarrow ^3\text{He}\eta$  is simulated by using the experimental angular distribution from Refs. [39,40]. The angular distribution was also recently extracted from our data (see Ref. [41]). The decay  $\eta \rightarrow \pi^+\pi^-\pi^0$  ( $BR = 22.92(28)\%$  [11]) was simulated at the final stage by using the central values of the extracted experimental Dalitz plot parameters. The main physics background processes include the  $\eta \rightarrow \pi^+\pi^-\gamma$  ( $BR = 4.22(8)\%$  [11]) decay and the direct two- and three-pion production reactions,  $pd \rightarrow ^3\text{He}\pi^+\pi^-$  and  $pd \rightarrow ^3\text{He}\pi^+\pi^-\pi^0$ . For the  $\eta \rightarrow \pi^+\pi^-\gamma$  reaction we used the results reported in [42,43]. All other  $\eta$  decay channels contribute marginally to the final result and may therefore be neglected. The direct  $3\pi$  production channel data simulated with uniform phase space distributions were modified to reproduce our final  $MM(^3\text{He})$  distribution as extracted from Fig. 3.

The chance coincidental events for the 16 most prominent  $pd$  reaction channels (with a total cross section of 80 mb) and the effect of energy pile-up in the different detector elements are also included in the simulation. Their relative strengths of the different channels are assumed by using the Fermi statistical model. For the quasifree breakup reactions the relative momentum between the  $np$  pair is simulated by using the deuteron wave function while for all other channels uniform phase space is assumed.

The accelerator and the target pellet beam overlap region is 3.8 mm in the horizontal direction and 5 mm in the vertical direction. The interaction point distribution can have tails in the  $z$  direction since the accelerator beam can also interact with a small fraction of the surrounding rest gas or divergent pellets. The shape of the tails is based on the  $z$ -vertex distribution deduced from experimental data with  $^3\text{He}$  production.

### C. Event selection

The signature of an event, in addition to the  $^3\text{He}$  ion reconstructed in the FD, is at least two tracks from charged particles in the MDC and at least two clusters in the calorimeter not associated with the tracks. The polar angles of charged particles detected in the MDC are greater than  $30^\circ$  and less than  $150^\circ$ . The time window in the CD with respect to the time signal of  $^3\text{He}$  is 6.2 ns for the charged particle tracks and 30 ns for a neutral particle hit. All possible combinations of tracks in the event is greater than the expected number of final-state particles.

The point of closest approach of the two charged particle tracks of the CD should be within 7 cm from the center of the pellet and the COSY beams overlap region. A kinematic fit with the

$$pd \rightarrow ^3\text{He}\pi^+\pi^-\gamma \quad (5)$$

reaction hypothesis is applied and the combination with the lowest  $\chi^2$  value is selected. A cut on the  $\chi^2$  probability is made at 1%. In the remaining analysis the variable values adjusted by the fit are used. The correlation between the fitted  $MM(^3\text{He})$  and the invariant mass of the two photons,  $IM(\gamma\gamma)$ , is shown in Fig. 2(a).

Figure 2(b) shows the extracted yield of the  $pd \rightarrow ^3\text{He}\eta$  events as a function of  $IM(\gamma\gamma)$ . The distribution was obtained by creating  $2 \text{ MeV}/c^2$  horizontal slices of the scatter plot in Fig. 2(a) and determining the peak content of each one. The resulting distribution agrees well with simulations of the  $\eta \rightarrow \pi^+\pi^-\pi^0$  and  $\eta \rightarrow \pi^+\pi^-\gamma$  decays. The relative normalization between the two decays is fixed by their branching ratios. For the final data sample only events with  $IM(\gamma\gamma) > 100 \text{ MeV}/c^2$  are selected.

The data sample used in this analysis consists of  $1.74 \times 10^5 \eta$  candidates. The comparison of the simulated and experimental distributions of  $MM(^3\text{He})$  is shown in Fig. 3. The dominating background comes from direct three-pion production. The contributions from two-pion production and the  $\eta \rightarrow \pi^+\pi^-\gamma$  decay are less than 1%.

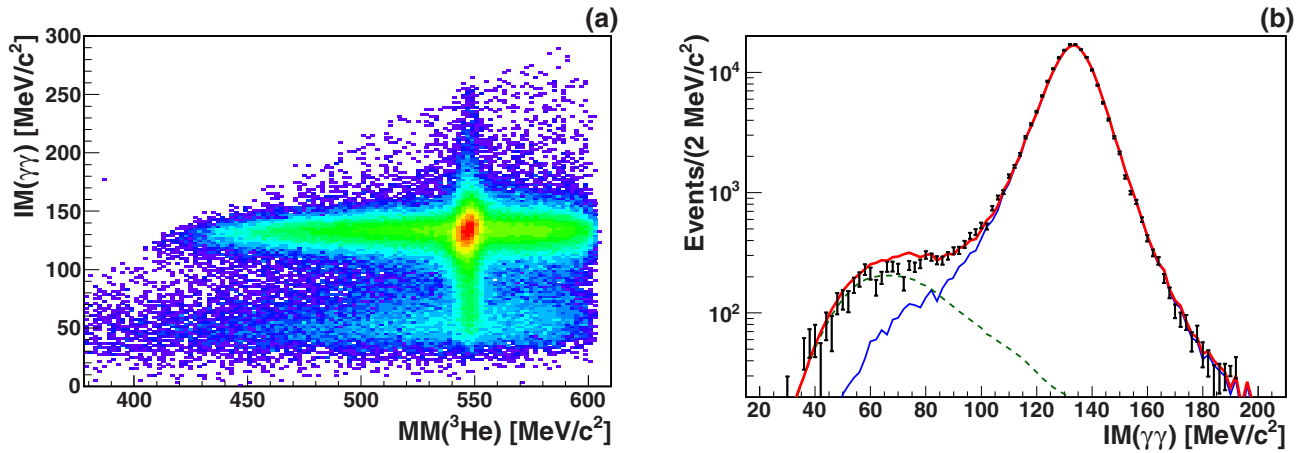


FIG. 2. (Color online) (a) Correlation between  $MM(^3\text{He})$  and  $IM(\gamma\gamma)$  for variables adjusted by a kinematic fit. (b) Comparison of the experimental and simulated contributions of the  $\eta$  events as a function of  $IM(\gamma\gamma)$ . The extracted number of the events in the  $\eta$  peak for each 2 MeV/c<sup>2</sup>  $IM(\gamma\gamma)$  slice is well described by the simulation (thick solid red line) including the  $\eta \rightarrow \pi^+\pi^-\pi^0$  (solid blue line) and  $\eta \rightarrow \pi^+\pi^-\gamma$  decays (dashed green line).

### III. RESULTS

The variables  $X$  and  $Y$  are calculated from Eq. (2) using the kinetic energies of the charged pions after the kinematic fitting boosted to the rest frame of the  $\pi^+\pi^-\gamma\gamma$  system. For the variables after the kinematic fit of the reaction (5) one has  $\mu \equiv IM(\pi^+\pi^-\gamma\gamma) = MM(^3\text{He})$ . However,  $\mu$  is not constrained to equal  $m_\eta$  and  $IM(\gamma\gamma)$  is not constrained to  $m_0$ . Therefore, the kinetic energy of the neutral pion,  $T_0$ , is determined in the following way:

$$T_0 = \mu - T_+ - T_- - 2m_\pm - IM(\gamma\gamma), \quad (6)$$

and for calculating  $Q_\eta$  we use Eq. (3).

The selected Dalitz plot bin width in  $X$  and  $Y$  ( $\Delta X = \Delta Y = 0.2$ ) is in our case limited by the statistics needed for background subtraction and reliable systematical crosschecks.

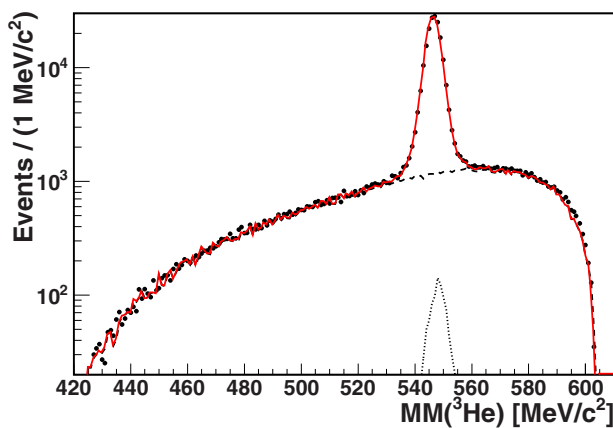


FIG. 3. (Color online) The distribution of  $MM(^3\text{He})$  using variables adjusted by the kinematic fit for the final data sample (dots), showing good agreement with the sum of the Monte Carlo distributions for the signal and the backgrounds (red solid line). Separately are shown contributions from  $\eta \rightarrow \pi^+\pi^-\gamma$  (dotted line) and from the direct  $3\pi$  production (dashed line).

The uncertainty of the  $X$  and  $Y$  measurement is well within the experimental resolution (with FWHM of approximately 0.10 for both  $\Delta X$  and  $\Delta Y$  in average). The  $X, Y$  region  $[-1.1, 1.1] \times [-1.1, 1.1]$  is divided into  $11 \times 11$  bins. The border bins with less than 90% Dalitz plot area inside the kinematic boundaries are excluded, leading to 59 bins used in the analysis. The definition and numbering scheme of the bins is given in Fig. 4.

The Dalitz plot for the  $\eta \rightarrow \pi^+\pi^-\pi^0$  decay is obtained by dividing the reconstructed  $X$  and  $Y$  variables into bins and determining the signal content in each bin from the corresponding  $\mu$  distribution. The signal content in each bin is estimated by a least-squares fit of the simulated data of

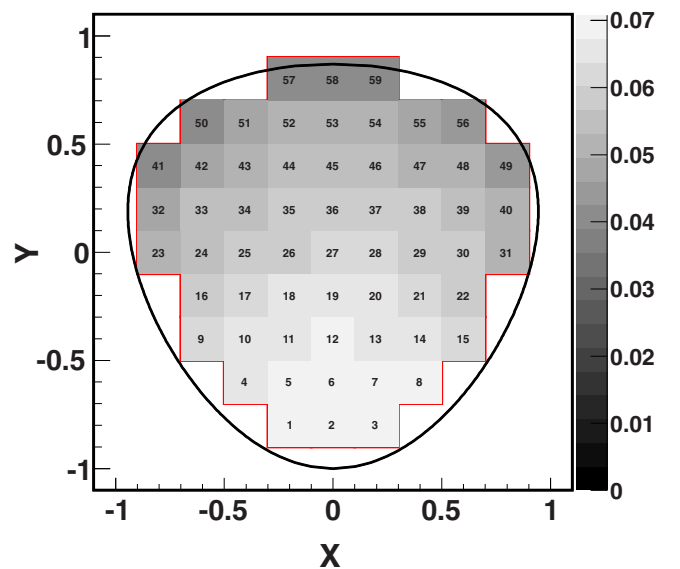


FIG. 4. (Color online) Position and numbering of the Dalitz plot bins used for the analysis. The acceptance for the  $\eta \rightarrow \pi^+\pi^-\pi^0$  decay is also indicated by the gray scale.

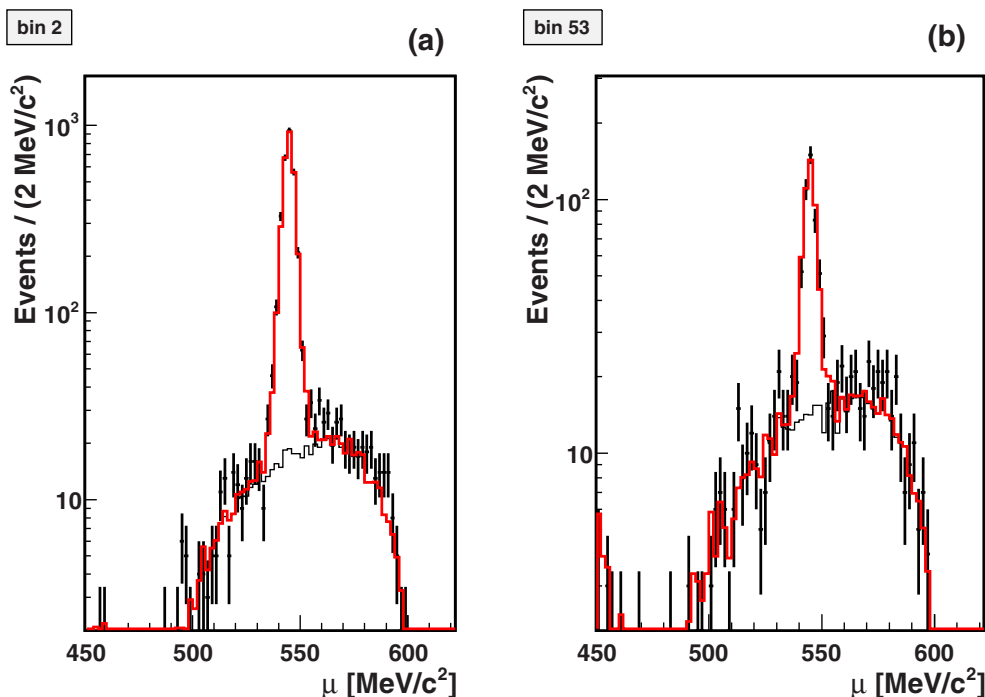


FIG. 5. (Color online) Two examples of the fits to the  $dN/d\mu$  distributions for a higher statistics Dalitz plot bin (a) and a low-statistics one (b). The red thick line is the fitted function from Eq. (7) while the thin line represents the continuous background contribution.

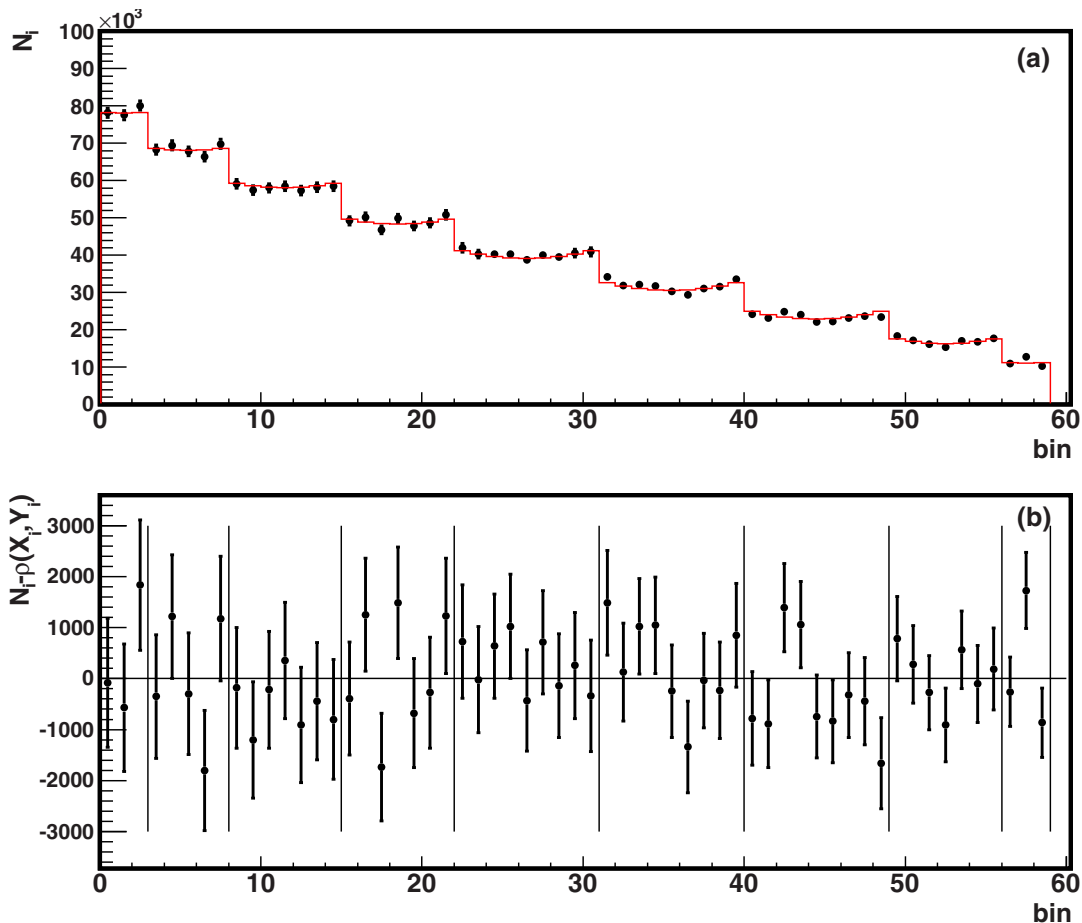


FIG. 6. (Color online) (a) Acceptance-corrected Dalitz plot bin contents with statistical uncertainties (black points with error bars) compared to the fitted function  $\rho(X, Y)$  (red line) for each bin. (b) The corresponding residuals.

TABLE III. Fit results for different sets of Dalitz plot parameters. The normalization factor,  $N$ , is omitted from the table. A number followed by '(fix)' means that the corresponding parameter was fixed to this number.

	$a$	$b$	$d$	$f$	$\chi^2/\text{dof}$
4 parameters (std)	-1.144(18)	0.219(19)	0.086(18)	0.115(37)	49.4/54
3 parameters	-1.101(11)	0.234(19)	0.078(18)	0 (fix)	58.8/55
2 parameters	-1.075(9)	0.201(17)	0 (fix)	0 (fix)	78.3/56

$pd \rightarrow {}^3\text{He}\eta$  and the  $pd \rightarrow {}^3\text{He}\pi^+\pi^-\pi^0$  continuum background reaction. The matrix element squared of the background reaction is assumed to be a linear function of  $\mu$  for each Dalitz plot bin  $i$ :

$$F_i(\mu) = N_S^i s_i(\mu) + N_B^i (1 + \alpha_i \mu) b_i(\mu), \quad (7)$$

where  $s_i(\mu)$  is the normalized,  $\int s_i(\mu) d\mu = 1$ ,  $pd \rightarrow {}^3\text{He}\eta$  signal distribution obtained from the  $pd \rightarrow {}^3\text{He}(\eta \rightarrow \pi^+\pi^-\pi^0)$  simulation.  $N_S^i$  is the number of the  $pd \rightarrow {}^3\text{He}\eta$  events in the experimental data in the  $i$ th Dalitz plot bin. The  $b_i(\mu)$  have the corresponding meaning with respect to the flat phase-space simulation of the  $pd \rightarrow {}^3\text{He}\pi^+\pi^-\pi^0$  reaction.  $N_S^i$ ,  $N_B^i$ , and  $\alpha_i$  are free parameters in the fit.

Two examples of the fits are shown in Fig. 5: one for a Dalitz plot bin with higher statistics (bin #2, centered at  $X = 0$ ,  $Y = -0.8$ ) and one for a bin with lower statistics (bin #53, centered at  $X = 0$ ,  $Y = 0.6$ ).

Finally, the simulated background from  $\eta \rightarrow \pi^+\pi^-\gamma$  events is subtracted from  $N_S^i$ . This contribution is small compared to the statistical uncertainties. The extracted number of  $\eta \rightarrow 3\pi$  events is corrected for acceptance. It was checked that the use of a bin-by-bin acceptance correction (i.e., diagonal smearing matrix) does not introduce any significant systematic effect.

The acceptance values, indicated in Fig. 4, are obtained from a MC sample of  $5 \times 10^7$   $\eta \rightarrow \pi^+\pi^-\pi^0$  events and varies between 4% and 7%. It is larger when  $T_0$  is small (i.e., lower  $Y$  values) but also when the kinetic energies of the two charged pions are similar (i.e., for  $X$  close to zero). Figure 6 shows the acceptance-corrected number of  $\eta \rightarrow \pi^+\pi^-\pi^0$  events as a function of the Dalitz plot bin number.

The Dalitz plot parameters are obtained with the least-squares fitting procedure which minimizes

$$\chi^2 = \sum_{i=1}^{59} \left( \frac{N_i - \rho(X_i, Y_i)}{\Delta N_i} \right)^2. \quad (8)$$

$N_i$  and  $\Delta N_i$  denote the acceptance-corrected number of events and their statistical uncertainty for the Dalitz plot bins ( $i = 1, \dots, 59$ ), respectively. The function  $\rho(X_i, Y_i)$ , defined in Eq. (4), is evaluated at the center of each Dalitz plot bin:  $X_i$  and  $Y_i$ . In our case the systematic effects introduced by this procedure are negligible as it was checked using the MC data sample. The overall normalization factor  $N$  is also a free parameter in the fit.

The obtained Dalitz plot parameters together with their statistical uncertainties are presented in Table III for different assumptions about the Dalitz plot parameters together with the fit  $\chi^2$  and number of degrees of freedom (dof). The  $c$

and  $e$  parameters are fixed to 0 in the fits. In addition, we have performed fits including these parameters. The result gives  $c$  and  $e$  consistent with zero [ $c = -0.007(9)$  and  $e = -0.020(23)$ ] and does not affect other parameters. For the case when all  $a$ ,  $b$ ,  $c$ ,  $d$ ,  $e$ , and  $f$  parameters are fit one obtains  $\chi^2/\text{dof} = 46.6/52$ . The correlation matrix between the fitted parameters for the standard result obtained is shown in Table IV.

Table IV shows a strong anticorrelation between the parameters  $a$  and  $f$ , which is also reflected in the uncertainties of the parameter  $a$ . The bins of the Dalitz plot are compared in Fig. 6 to the parametrization with four free parameters  $a$ ,  $b$ ,  $d$ , and  $f$  where the remaining ones are set to zero (the parametrization labeled as std in Table III).

#### IV. SYSTEMATIC UNCERTAINTIES

The systematic uncertainties of the obtained Dalitz plot parameters are investigated by including variations due to known sources of uncertainties in the MC-generated data and by changing the selection criteria to find the remaining effects. In particular, the consistency of extraction of the Dalitz plot distribution and fitting of the Dalitz plot parameters were tested by using MC-generated data 10 times larger than in the experiment. The input parameters were reproduced without introducing any systematical deviation within the statistical uncertainties.

One of the most important sources of systematical uncertainties is the direct background subtraction procedure. This uncertainty is estimated by comparing a fit with the signal region excluded from the fit, and the signal term  $N_S^i s_i(\mu)$  in Eq. (7) is omitted and the background is subtracted directly from the data ([Test 1] in Table V).

To investigate further possible systematical effects the data sample has been divided into sets of high and low luminosity. The  $pd \rightarrow X$  cross section is  $\sim 80$  mb, which amounts to a few background reactions produced per  $\mu s$ . The largest effect is connected to the calorimeter signals since the decay times are of the order of  $\mu s$ . The Dalitz plot parameter values obtained

TABLE IV. Correlation matrix for the Dalitz plot parameters.

	$a$	$b$	$d$
$b$	-0.24		
$d$	-0.45	0.36	
$f$	-0.79	-0.25	0.14

TABLE V. Dalitz plot parameters extracted for different tests for systematic effects.

	$-a$	$b$	$d$	$f$	$\chi^2/\text{dof}$
Standard result	1.144(18)	0.219(19)	0.086(18)	0.115(37)	49.4/54
[Test 1] Background fit	1.126(18)	0.230(19)	0.094(18)	0.111(37)	60.5/54
[Test 2] Low luminosity	1.130(24)	0.216(26)	0.059(24)	0.104(50)	50.5/54
[Test 2] High luminosity	1.164(25)	0.219(28)	0.106(26)	0.152(52)	54.9/54
[Test 3] RF	1.127(26)	0.177(28)	0.085(27)	0.140(55)	56.1/54
[Test 3] No RF	1.139(23)	0.252(26)	0.076(24)	0.069(49)	49.6/54
[Test 4] $P_{kf} > 0.1$	1.146(22)	0.224(24)	0.075(22)	0.117(46)	48.0/54
[Test 5] $\theta_{3\text{He}} < 9.2^\circ$	1.148(25)	0.194(28)	0.081(27)	0.148(53)	47.5/54
[Test 5] $\theta_{3\text{He}} > 9.2^\circ$	1.126(25)	0.215(28)	0.067(25)	0.098(53)	63.9/54
[Test 6] $T_{3\text{He}} < 340$ MeV	1.151(22)	0.183(24)	0.114(24)	0.157(46)	43.8/54
[Test 6] $T_{3\text{He}} > 340$ MeV	1.175(27)	0.261(30)	0.071(27)	0.130(57)	46.4/54

for the low- and high-luminosity samples are shown by [Test 2] in Table V.

Two different accelerator beam modes were used during the beam time and they cover roughly equal time of data taking. In the first half, a constant beam energy during the accelerator cycle was assured by a fixed radio frequency (RF). In the second half, a coasting beam with the RF switched off swept the target, leading to a slight decrease of the beam energy during a cycle (from 1000.0 to 993.5 MeV). In the experimental analysis this energy decrease is taken into account. However, in the simulations the acceptance has been calculated for a beam kinetic energy fixed at 1 GeV. The comparison of the two cases ([Test 3] in Table V) shows the largest deviation for the  $b$  parameter ( $\approx 2\sigma$ ). To investigate the source of the effect we have calculated the acceptances also for the lowest beam energy in the RF-off mode (993.5 MeV) and concluded that the change is too small to explain the observed deviation.

The effect of the uncertainty of the implemented detector resolution in the detector simulations is tested by increasing the kinematic fit probability,  $P_{kf}$ , from 0.01 to 0.1 ([Test 4] in

Table V). The differences between the parameter values are not significant and are therefore neglected in the final systematic uncertainty.

The result should not depend on the  $^3\text{He}$  scattering angle ( $\theta_{3\text{He}}$ ) or on the angle of the  $\eta$  meson in the center-of-mass system (equivalent to the  $^3\text{He}$  energy in the laboratory system:  $T_{3\text{He}}$ ). Two additional tests were carried out by dividing the data sample with respect to the two variables with cut values  $\theta_{3\text{He}} = 9.2^\circ$  ([Test 5]) and  $T_{3\text{He}} = 340$  MeV ([Test 6]) selected in a way that the corresponding subsamples have the same statistics. The [Test 5] shows no significant deviations for the extracted Dalitz plot parameters while for the [Test 6] a deviation of  $2\sigma$  is observed for the  $b$  parameter.

The significant systematic changes are seen only for the parameters  $b$  ([Test 3] and [Test 6]) and  $d$  ([Test 2]); we use the methodology of Ref. [44] with a  $1\sigma$  threshold for the test significance. The systematic uncertainty is estimated as one half of the difference between the parameter values for the two subsets in the relevant tests. The statistical uncertainty due to the number of events in the subsets is unfolded from

TABLE VI. Acceptance-corrected Dalitz plot distribution. The bin numbering is given in Fig. 4. The bin contents are normalized to the bin centered at  $X = 0, Y = 0$  (bin #27).

Bin #	Content						
1	$2.020 \pm 0.033$	16	$1.271 \pm 0.029$	31	$1.058 \pm 0.028$	46	$0.573 \pm 0.021$
2	$2.004 \pm 0.032$	17	$1.296 \pm 0.029$	32	$0.883 \pm 0.027$	47	$0.597 \pm 0.022$
3	$2.069 \pm 0.033$	18	$1.209 \pm 0.027$	33	$0.824 \pm 0.025$	48	$0.611 \pm 0.022$
4	$1.764 \pm 0.031$	19	$1.289 \pm 0.028$	34	$0.830 \pm 0.024$	49	$0.604 \pm 0.023$
5	$1.794 \pm 0.031$	20	$1.236 \pm 0.028$	35	$0.820 \pm 0.024$	50	$0.473 \pm 0.021$
6	$1.752 \pm 0.031$	21	$1.257 \pm 0.028$	36	$0.783 \pm 0.024$	51	$0.443 \pm 0.020$
7	$1.716 \pm 0.031$	22	$1.313 \pm 0.029$	37	$0.758 \pm 0.023$	52	$0.418 \pm 0.019$
8	$1.804 \pm 0.032$	23	$1.085 \pm 0.029$	38	$0.802 \pm 0.024$	53	$0.398 \pm 0.019$
9	$1.528 \pm 0.031$	24	$1.042 \pm 0.027$	39	$0.815 \pm 0.025$	54	$0.440 \pm 0.020$
10	$1.484 \pm 0.029$	25	$1.041 \pm 0.026$	40	$0.867 \pm 0.026$	55	$0.433 \pm 0.020$
11	$1.499 \pm 0.030$	26	$1.041 \pm 0.026$	41	$0.626 \pm 0.024$	56	$0.458 \pm 0.021$
12	$1.511 \pm 0.030$	27	$1.000 \pm 0.026$	42	$0.600 \pm 0.022$	57	$0.283 \pm 0.018$
13	$1.481 \pm 0.029$	28	$1.033 \pm 0.026$	43	$0.641 \pm 0.022$	58	$0.331 \pm 0.019$
14	$1.504 \pm 0.030$	29	$1.021 \pm 0.026$	44	$0.622 \pm 0.022$	59	$0.268 \pm 0.018$
15	$1.512 \pm 0.030$	30	$1.049 \pm 0.027$	45	$0.572 \pm 0.021$		

the obtained estimate. The final result for the Dalitz plot parameters is expressed in the following way:

$$\begin{aligned} -a &= 1.144 \pm 0.018(\text{stat}), \\ b &= 0.219 \pm 0.019(\text{stat}) \pm 0.047(\text{syst}), \\ d &= 0.086 \pm 0.018(\text{stat}) \pm 0.015(\text{syst}), \\ f &= 0.115 \pm 0.037(\text{stat}). \end{aligned}$$

In addition, we give the values for the C-violating parameters  $c$  and  $e$ :

$$\begin{aligned} c &= -0.007 \pm 0.009(\text{stat}), \\ e &= -0.020 \pm 0.023(\text{stat}) \pm 0.029(\text{syst}). \end{aligned}$$

The results are generally dominated by statistical uncertainties and therefore the provided table with acceptance-corrected bin contents, Table VI, could be used directly for comparison with theoretical models.

## V. DISCUSSION OF RESULTS

Parameters  $a$ ,  $b$ , and  $d$  significantly deviate from zero. The  $d$  parameter is  $3.7\sigma$  above zero. From Table III it is seen that  $\chi^2$  per dof is only slightly worse if parameter  $f$  is set to zero in the fit. The significance of allowing  $f \neq 0$  in our data is  $3.1\sigma$ . However, the  $a$  and  $f$  parameters are strongly anticorrelated (see Table IV), and excluding  $f$  from the fit affects also the  $a$  value. The data do not require higher order terms in the polynomial expansion such as  $g \cdot X^2Y$  and  $h \cdot X^3$ .

Here we list deviations from the Dalitz plot parameters obtained by the KLOE Collaboration [26] together with their significance (with statistical and systematic uncertainties added in squares):

$$\begin{aligned} -\Delta a &= +0.054(23) (+2.3\sigma), \\ \Delta b &= +0.095(44) (+1.8\sigma), \end{aligned}$$

$$\Delta d = +0.029(28) (+1.1\sigma),$$

$$\Delta f = -0.025(43) (-0.6\sigma).$$

Our results are generally consistent with those of KLOE; however, there is some tension for  $a$  and  $b$  parameters. Our data confirm the discrepancies between theoretical calculations and the experimental values from the KLOE experiment. The provided experimental data points of the individual Dalitz plot bins will allow independent analyses using NREFT or dispersive methods.

The presented results are based on the first part of the WASA-at-COSY data from the  $pd \rightarrow {}^3\text{He}\eta$  reaction. More data are available from WASA-at-COSY also from the  $pp \rightarrow pp\eta$  reaction. Together with expected results from other experiments the goal of a precise determination of the  $\eta \rightarrow \pi^+\pi^-\pi^0$  Dalitz plot parameters might soon be reached.

## ACKNOWLEDGMENTS

This work was supported in part by the EU Integrated Infrastructure Initiative Hadron Physics Project under Contract No. RII3-CT-2004-506078; by the European Commission under the 7th Framework Programme through the ‘‘Research Infrastructures’’ action of the ‘‘Capacities’’ Programme, Call: FP7-INFRASTRUCTURES-2008-1, Grant Agreement No. 227431; and by the Polish National Science Centre through Grants No. 86/2/N-DFG/07/2011/00320/B/H03/2011/40, No. 2011/01/B/ST2/00431, No. 2011/03/B/ST2/01847, and No. 0312/B/H03/2011/40 and the Foundation for Polish Science. We gratefully acknowledge the support given by the Swedish Research Council, the Knut and Alice Wallenberg Foundation, and the Forschungszentrum Jülich FFE Funding Program of the Jülich Center for Hadron Physics. This work is based on the Ph.D. thesis of Patrik Adlarson supported by Uddeholms Forskarstipendium.

- 
- [1] D. Sutherland, *Phys. Lett.* **23**, 384 (1966).
  - [2] R. Baur, J. Kambor, and D. Wyler, *Nucl. Phys. B* **460**, 127 (1996).
  - [3] C. Ditsche, B. Kubis, and U.-G. Meissner, *Eur. Phys. J. C* **60**, 83 (2009).
  - [4] H. Leutwyler, *Phys. Lett. B* **378**, 313 (1996).
  - [5] D. B. Kaplan and A. V. Manohar, *Phys. Rev. Lett.* **56**, 2004 (1986).
  - [6] D. Babusci *et al.* (KLOE-2 Collaboration), *J. High Energy Phys.* **01** (2013) 119.
  - [7] J. Bell and D. Sutherland, *Nucl. Phys. B* **4**, 315 (1968).
  - [8] J. A. Cronin, *Phys. Rev.* **161**, 1483 (1967).
  - [9] J. Gasser and H. Leutwyler, *Nucl. Phys. B* **250**, 539 (1985).
  - [10] J. Bijnens and K. Ghorbani, *J. High Energy Phys.* **11** (2007) 030.
  - [11] J. Beringer *et al.* (Particle Data Group), *Phys. Rev. D* **86**, 010001 (2012).
  - [12] C. Roiesnel and T. N. Truong, *Nucl. Phys. B* **187**, 293 (1981).
  - [13] A. Anisovich and H. Leutwyler, *Phys. Lett. B* **375**, 335 (1996).
  - [14] J. Kambor, C. Wiesendanger, and D. Wyler, *Nucl. Phys. B* **465**, 215 (1996).
  - [15] K. Kampf, M. Knecht, J. Novotny, and M. Zdrahal, *Phys. Rev. D* **84**, 114015 (2011).
  - [16] S. Aoki *et al.*, [arXiv:1310.8555](https://arxiv.org/abs/1310.8555) [hep-lat].
  - [17] D. Alde *et al.* (Serpukhov-Brussels-Annecy (LAPP) Collaboration, Soviet-CERN Collaboration), *Z. Phys. C* **25**, 225 (1984).
  - [18] A. Abele *et al.* (Crystal Barrel), *Phys. Lett. B* **417**, 193 (1998).
  - [19] M. Achasov *et al.*, *JETP Lett.* **73**, 451 (2001).
  - [20] W. Tippens *et al.* (Crystal Ball Collaboration), *Phys. Rev. Lett.* **87**, 192001 (2001).
  - [21] M. Bashkanov *et al.* (CELSIUS/WASA), *Phys. Rev. C* **76**, 048201 (2007).
  - [22] C. Adolph *et al.* (WASA-at-COSY Collaboration), *Phys. Lett. B* **677**, 24 (2009).
  - [23] S. Prakhov *et al.* (Crystal Ball at MAMI and A2 Collaborations), *Phys. Rev. C* **79**, 035204 (2009).
  - [24] M. Unverzagt *et al.* (Crystal Ball at MAMI, TAPS and A2 Collaborations), *Eur. Phys. J. A* **39**, 169 (2009).

- [25] F. Ambrosino *et al.* (KLOE Collaboration), *Phys. Lett. B* **694**, 16 (2010).
- [26] F. Ambrosino *et al.* (KLOE Collaboration), *J. High Energy Phys.* **05** (2008) 006.
- [27] G. Colangelo, S. Lanz, and E. Passemar, *PoS CD09*, 047 (2009).
- [28] G. Colangelo, J. Gasser, B. Kubis, and A. Rusetsky, *Phys. Lett. B* **638**, 187 (2006).
- [29] C.-O. Gullstrom, A. Kupsc, and A. Rusetsky, *Phys. Rev. C* **79**, 028201 (2009).
- [30] S. P. Schneider, B. Kubis, and C. Ditsche, *J. High Energy Phys.* **02** (2011) 028.
- [31] B. Borasoy and R. Nissler, *Eur. Phys. J. A* **26**, 383 (2005).
- [32] J. Bijnens and J. Gasser, *Phys. Scr. T* **99**, 34 (2002).
- [33] M. Gormley *et al.*, *Phys. Rev. D* **2**, 501 (1970).
- [34] J. Layter *et al.*, *Phys. Rev. D* **7**, 2565 (1973).
- [35] A. Abele *et al.* (Crystal Barrel Collaboration), *Phys. Lett. B* **417**, 197 (1998).
- [36] C. Bargholtz *et al.* (CELSIUS/WASA), *Nucl. Instrum. Methods A* **594**, 339 (2008).
- [37] H. H. Adam *et al.* (WASA-at-COSY), [arXiv:nucl-ex/0411038](https://arxiv.org/abs/nucl-ex/0411038).
- [38] R. Maier, *Nucl. Instrum. Methods A* **390**, 1 (1997).
- [39] R. Bilger *et al.*, *Phys. Rev. C* **65**, 044608 (2002).
- [40] T. Rausmann *et al.* (ANKE Collaboration), *Phys. Rev. C* **80**, 017001 (2009).
- [41] P. Adlarson *et al.* (WASA-at-COSY Collaboration), *Eur. Phys. J. A* **50**, 100 (2014).
- [42] P. Adlarson *et al.* (WASA-at-COSY Collaboration), *Phys. Lett. B* **707**, 243 (2012).
- [43] D. Babusci *et al.* (KLOE Collaboration), *Phys. Lett. B* **718**, 910 (2013).
- [44] R. Barlow, [arXiv:hep-ex/0207026](https://arxiv.org/abs/hep-ex/0207026) [hep-ex].